

Basis adaptation for the stochastic nonlinear Poisson–Boltzmann equation

Amirreza Khodadadian¹ · Clemens Heitzinger^{1,2}

© Springer Science+Business Media New York 2016

Abstract A basis-adaptation method based on polynomial chaos expansion is used for the stochastic nonlinear Poisson–Boltzmann equation. The uncertainty in this numerical approach is motivated by the quantification of noise and fluctuations in nanoscale field-effect sensors. The method used here takes advantage of the properties of the nonlinear Poisson–Boltzmann equation and shows an exact and efficient approximation of the real solution. Numerical examples are motivated by the quantification of noise and fluctuations in nanowire field-effect sensors as a concrete example. Basis adaptation is validated by comparison with the full solution, and it is compared to optimized multi-level Monte-Carlo method, and the model equations are validated by comparison with experiments. Finally, various design parameters of the field-effect sensors are investigated in order to maximize the signal-to-noise ratio.

Keywords Poisson–Boltzmann equation · Current · Biological noise · Polynomial chaos expansion · Biosensor

1 Introduction

A basis-adaptation method for the stochastic nonlinear Poisson–Boltzmann equation is applied. Here the main

sources of randomness in the stochastic version of the nonlinear Poisson–Boltzmann equation are random permittivities and random charge concentrations near the sensor surface. Because the number of dimensions describing the random permittivity and charge concentration is large in realistic applications, a reduction of the computational complexity is essential and this goal is achieved by the basis-adaptation approach presented here. The quantity of interest is the current through the transducer subdomain, which can be calculated by a nonlinear functional in the graded-channel approximation.

The Poisson–Boltzmann equation, whose stochastic version is the basic model equation here, is one of the most important equations in computational chemistry. The equation models the electrostatic potential in any application where screening by free ions in a liquid occurs. It also describes screening in a semiconductor. A concrete physical realization of the model equation are affinity-based field-effect sensors. In the numerical examples shown here, nanowire field-effect biosensors are simulated, and the expected values, standard deviations, and signal-to-noise ratios are calculated.

Affinity-based sensors, in particular the recently experimentally demonstrated nanowire field-effect sensors, pose demanding numerical problems because of the large number of stochastic dimensions. A cross section through a nanowire field-effect biosensor [10, 12, 15, 22, 26, 27, 34, 35, 42] is shown in Fig. 1, but the same principle also applies to gas sensors [6, 20, 31, 40]. The sensors are affinity-based, since the target molecules are only detected when they are sufficiently close to the sensor. The current through the semi-conducting silicon nanowire, which is the actual transducer, is measured. The conductance of the nanowire is modulated by the electrostatic potential, which—in turn—is changed when charged target molecules bind to the probe molecules

✉ Amirreza Khodadadian
amirreza.khodadadian@tuwien.ac.at

Clemens Heitzinger
clemens.heitzinger@asu.edu;
clemens.heitzinger@tuwien.ac.at

¹ Institute for Analysis and Scientific Computing, Vienna University of Technology (TU Vienna), Vienna, Austria

² School of Mathematical and Statistical Sciences, Arizona State University (ASU), Tempe, AZ, USA

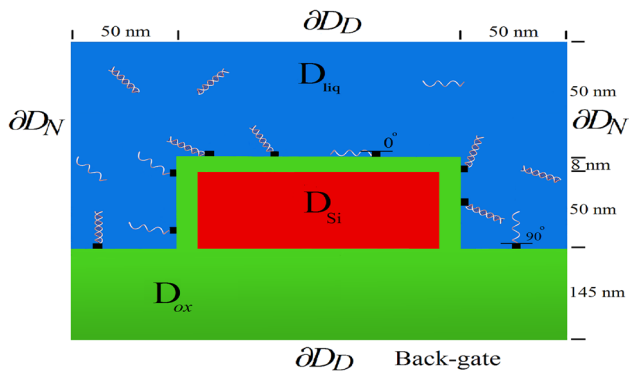


Fig. 1 Cross section through a field-effect nanowire sensor, showing subdomains and boundary conditions. In the electrolyte (D_{liq}), the random binding of target molecules to immobilized receptor molecules at the surface defines molecule subdomain (D_M)

functionalized at the surface of the sensor. The number of target molecules bound to probes at the sensor surface is random, since the target molecules bind to and dissociate from the probe molecules. The positions of the probe molecules, as well as their orientations and the orientations of the probe–target complexes are random. This type of noise is often called biological noise [16, 38]. The uncertainty domain (electrolyte and molecule subdomains) is shown in Fig. 1 as well. Each molecule or each probe molecule adds at least one stochastic dimension.

The concept of nanowire field-effect sensors is very general and has been applied to the detection of DNA, proteins such as tumor markers, and toxic gases such as carbon monoxide. The sensors offer advantages like miniaturization, high sensitivity, fast response, and low power consumption [12, 27, 35]. Furthermore, the target molecules do not have to be marked in field-effect sensors in contrast to the commonly used fluorescent or radioactive markers in other detection methods.

There are various sources of noise and fluctuations in affinity-based sensors, where the biological noise is one of the most prominent ones. Its quantification is essential for understanding the signal-to-noise ratio [33] and the detection limit of the sensors. Regarding the modeling, the randomness due to the biological noise at the sensor surface propagates through a partial differential equation (PDE) model and finally yields the sensor output. The model used in the present work, based on the stochastic nonlinear Poisson–Boltzmann equation and a functional for the quantity of interest, is described in detail in Sect. 2.

Previous work on the modeling and simulation of nanowire field-effect sensors has focused on deterministic equations. The inherent deterministic multiscale problem was solved in [18]. Existence and uniqueness of a self-consistent model was shown in [3], and a FETI algorithm was presented in [4]. A method for calculating the probabilities of the orienta-

tions of various molecules and hence the stochastic process was developed in [17]. The design of optimal sensors was discussed in [5], and the biological noise was modeled in [37, 38]. An effective equation for the covariance was found in [19] as the result of a homogenization approach. Nanowire field-effect biosensors were also modeled and simulated in [22, 28–30], where the alternating-current small-signal regime was considered.

The numerical approach developed here can also be applied to investigate various sources of noise and fluctuations in more traditional semiconductor devices such as MOSFETs and FinFETs. Random-dopant effects are one example [1, 8] and of great importance for integrated circuits consisting of nanoscale transistors. Another example is random telegraph noise (RTN) [23, 39]. It is caused by random trapping and de-trapping of charges at interface states and also of great importance for such small devices. By using stochastic partial differential equations, these effects can be modeled by stochastic coefficients analogously to the present work.

The rest of this paper is organized as follows: In Sect. 2, the stochastic Poisson–Boltzmann equation and the rest of the model are described explicitly. In Sect. 3, basis adaptation for this model is introduced in detail. In Sect. 4, optimal multi-level Monte Carlo is shortly described and serves as a comparison. Numerical results are presented in Sect. 5. Finally, conclusions are drawn in Sect. 6.

2 The model equations

2.1 The stochastic nonlinear Poisson–Boltzmann equation

The main model equation is the stochastic nonlinear Poisson–Boltzmann equation:

$$-\nabla \cdot (A(x, y, \omega) \nabla u(x, y, \omega)) = \begin{cases} q(C_{dop}(x, y, \omega) + p(x, y, \omega) - n(x, y, \omega)) & \text{in } D_{Si}, \\ 0 & \text{in } D_{ox}, \\ \rho(x, y, \omega) & \text{in } D_M, \\ -2\varphi(x, y, \omega) \sinh(\beta(u(x, y, \omega) - \Phi_F(x, y, \omega))) & \text{in } D_{liq}, \end{cases} \quad (1a)$$

$$u(0+, y, \omega) - u(0-, y, \omega) = \alpha(y, \omega) \quad \text{on } \Gamma, \quad (1b)$$

$$A(0+) \partial_x u(0+, y, \omega) - A(0-) \partial_x u(0-, y, \omega) = \chi(y, \omega) \quad \text{on } \Gamma, \quad (1c)$$

$$u(x, y, \omega) = u_D(x, y) \quad \text{on } \partial D_D, \quad (1d)$$

$$\nabla_n u(x, y, \omega) = 0 \quad \text{on } \partial D_N. \quad (1e)$$

Here, u is the electrostatic potential, A is the permittivity function, φ is the ion accessibility function, Φ_F is the Fermi level, ρ describes the fixed (surface) charges of mole-

cules, and C_{dop} is the doping concentration. Furthermore, (Ω, Σ, P) is a probability space and $\omega \in \Omega$ is a set of independent Gaussian random variables. The domain $D \subset \mathbb{R}^2$ is depicted in Fig. 1. It is partitioned into the four subdomains, i.e., D_{Si} (silicon), D_{ox} (oxide), D_{liq} (liquid), and D_{M} (molecule) with the interface Γ between D_{ox} and D_{liq} . The silicon nanowire is always covered by a thin layer of silicon oxide (D_{ox}) and surrounded by the liquid containing the target molecules. The subdomain D_{M} is defined when in the liquid the charged target molecules bind to the probe molecules at oxide (insulator) surface. The relative permittivities of the subdomains are $A_{\text{Si}} = 11.7$, $A_{\text{ox}} = 3.9$, $A_{\text{M}} = 3.7$, and $A_{\text{liq}} = 78.4$. Furthermore, $q > 0$ is the elementary charge, and the constant β is defined as $\beta := q/(k_{\text{B}}T)$ in terms of the Boltzmann constant k_{B} and the temperature T . In the simulations performed here, a thermal voltage of 0.021 V was used. The concentration $p(x, y, \omega)$ of positive free charge carriers and the concentration $n(x, y, \omega)$ of negative ones are given by Boltzmann distributions as

$$p(x, y, \omega) = \kappa_i \exp\left(-\frac{q(u(x, y, \omega) - \Phi_{\text{F}})}{k_{\text{B}}T}\right), \quad (2a)$$

$$n(x, y, \omega) = \kappa_i \exp\left(\frac{q(u(x, y, \omega) - \Phi_{\text{F}})}{k_{\text{B}}T}\right). \quad (2b)$$

Here, the constant κ_i is the intrinsic carrier concentration n_i of the semiconductor ($1.5 \times 10^{10} \text{ cm}^{-3}$) or the bulk ionic concentration [7] in the electrolyte.

The discontinuities or interface conditions in the electrostatic potential arise from homogenization [18]. At the interface Γ between the silicon oxide and the liquid, the charge concentration exhibits a rapidly oscillating spatial structure which leads to a multiscale problem [18]. The continuity conditions (1b) and (1c) are due to the jump in the permittivity A between two different materials. Here, $0+$ denotes the limit at the interface on the side of the liquid, while $0-$ is the limit on the side of the silicon oxide layer. The two interface conditions mean that the rapidly oscillating charge concentration in the surface layer is described by the macroscopic dipole moment density α and the macroscopic surface charge density χ [4].

The boundary conditions in (1), as illustrated in Fig. 1, are Dirichlet boundary conditions (∂D_{D}) and Neumann boundary condition (∂D_{N}). A voltage across the simulation domain in the vertical direction can be applied as well by an electrode in the liquid (solution voltage) and by a back-gate contact at the bottom of the structure (back-gate voltage). These are also part of ∂D_{D} . Zero Neumann boundary conditions hold on the Neumann part ∂D_{N} of the boundary.

In crystals of pure silicon, the number density of electrons in the conduction band and of holes in the valence band are equal, and therefore the Fermi level as a function of doping concentration can be calculated for electrons and holes as

$$\Phi_{\text{F}} = E_{\text{c}} + k_{\text{B}}T \ln \frac{n}{n_i} = E_{\text{c}} - k_{\text{B}}T \ln \frac{p}{n_i},$$

where E_{c} is the minimum energy of the conduction band in the semiconductor and n_i is again the intrinsic carrier concentration of silicon. The equation holds true because $pn = n_i^2$.

2.2 The quantity of interest and the graded-channel approximation

Solving the Poisson–Boltzmann equation (1) yields the electrostatic potential on a cross section of the structure as shown in Fig. 1, from which the current through the sensor can be calculated by the graded-channel approximation as in [17]. The graded-channel approximation can be derived from the drift-diffusion equations as follows:

$$\begin{aligned} \nabla \cdot J_n(x, y, \omega) &= qR(n(x, y, \omega), p(x, y, \omega)), \\ -\nabla \cdot J_p(x, y, \omega) &= qR(n(x, y, \omega), p(x, y, \omega)), \\ J_n(x, y, \omega) &= q(D_n \nabla n(x, y, \omega) \\ &\quad - \mu_n n(x, y, \omega) \nabla u(x, y, \omega)), \\ J_p(x, y, \omega) &= q(-D_p \nabla p(x, y, \omega) \\ &\quad - \mu_p p(x, y, \omega) \nabla u(x, y, \omega)), \end{aligned}$$

where n and p are the electron and hole concentrations; J_n and J_p are their current densities; D_n and D_p are their diffusion coefficients; and μ_n and μ_p are their mobilities. In addition, we use the popular Shockley–Read–Hall (SRH) recombination rate:

$$\begin{aligned} R(n(x, y, \omega), p(x, y, \omega)) \\ := \frac{n(x, y, \omega)p(x, y, \omega) - n_i^2}{\tau_p(n(x, y, \omega) + n_i) + \tau_n(p(x, y, \omega) + n_i)}. \end{aligned}$$

Two assumptions are necessary for the graded-channel approximation. The first assumption is that only the drift current, and not the diffusion current, plays a role. This yields the current density as

$$J^{\text{drift}} := J_n^{\text{drift}} + J_p^{\text{drift}} = -q\mu_n n \nabla u - q\mu_p p \nabla u.$$

The second assumption is that the electric field is constant along the z -axis of the sensor, i.e., $E = (u_{\text{S}} - u_{\text{D}})/Z$ holds, where $u_{\text{S}} - u_{\text{D}}$ is the potential difference between the two contacts (the source and the drain) with a distance Z apart. Since $E = -\partial_z u$, we hence find

$$J^{\text{drift}} = qE(\mu_n n + \mu_p p).$$

The total electrical current is now obtained by taking the integral

$$I(\omega) := f(u(x, y, \omega)) := \int J^{\text{drift}} dx dy$$

$$= qE \int (\mu_n n(x, y, \omega) + \mu_p p(x, y, \omega)) dx dy \quad (3)$$

with n and p from (2) over a cross section of the semiconducting part (D_{Si}) of the sensor. This is the quantity of interest that is recorded in measurements.

As we have seen, the graded-channel approximation is a simplification of the drift-diffusion–Poisson equations and neglects diffusion. Therefore, the full drift-diffusion–Poisson system is a better model for investigations in the subthreshold regime.

2.3 The random coefficients in the stochastic nonlinear Poisson–Boltzmann equation

The biological noise, i.e., the random movement of probe and target molecules at or near the surface of any affinity-based sensor, propagates through a PDE model of the sensor and results in noise in the sensor output. Biological noise is one of the major sources of noise and fluctuations in field-effect sensors; it is due to two effects: the random association of target molecules with probe molecules functionalized at the sensor surface and their random dissociation from the probe molecules as well as randomness in the orientation of any molecule bound to a surface. In order to quantify biological noise, the association and dissociation processes were modeled in [38], where the expected number and variance of the number of target molecules bound to probe molecules were calculated. The random orientations were modeled in [17], where the probabilities of the orientations were determined.

When any affinity-based sensor is manufactured, the probe molecules are functionalized at the sensor surface [32] at ran-

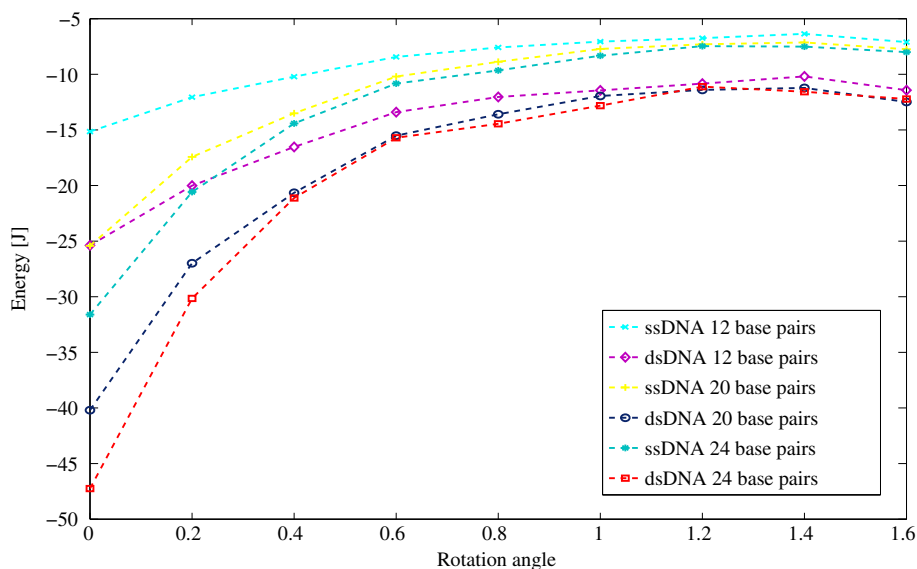
dom, but fixed locations. In other words, each probe molecule is a binding site that is occupied by a target molecule with a certain probability that can be determined [38]. Unspecific binding of target molecules to the sensor surface in the absence of probe molecules is also possible. Since this effect is not important in a well-designed sensor, it is not included here; however, it can be taken into account in the model in a straightforward manner.

The orientation of a charged molecule with respect to a charged surface is determined by the electrostatic free energy of the system. A method for determining the free energies of charged molecules as functions of various parameters was presented in [17]. First, the electrostatic free energy $E(\eta)$ is calculated as a function of the angle $\eta := (\eta_1, \eta_2)$, which represents the orientation of the molecule with respect to the surface. In general, each molecule has two degrees of freedom, although in the case of DNA oligomers their structure leads to a simplification and one angle $\eta := \eta_1 \in [0, \pi/2]$ is sufficient. Then a Boltzmann distribution is used to find the probability of a configuration as a function of the angle η . It is given by

$$P(\eta) = \frac{\exp(-E(\eta)/(k_B T))}{\int \exp(-E(\eta)/(k_B T)) d\eta} \propto \exp\left(-\frac{E(\eta)}{k_B T}\right). \quad (4)$$

Figure 2 shows a concrete example and the data used in the numerical examples in this paper. Electrostatic free energies for single- and double-stranded DNA oligomers of different lengths are shown. As the charge density of dsDNA is twice that of ssDNA, the binding energies of double-stranded DNA (dsDNA) oligomers are higher than their single-stranded (ssDNA) counterparts. The length of the oligomers decreases the free energy mostly for lower angles, i.e., for horizontal configurations, where electrostatic interactions with the sur-

Fig. 2 Electrostatic free energies of various ssDNA and dsDNA oligomers as a function of angle for a surface charge of -0.5 q nm^{-2} in a liquid with an ionic concentration of 30 mM. The angles are defined with respect to the surface, where 0 means a molecule parallel to the surface and $\pi/2$ means a molecule perpendicular to the surface (as indicated in Fig. 1). Data were obtained from [17]



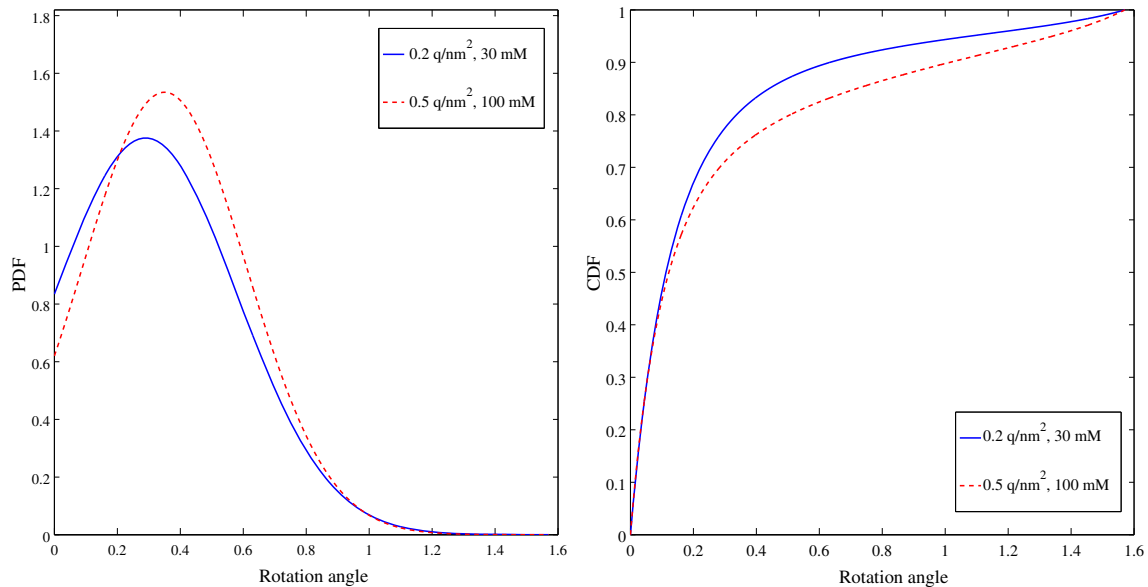


Fig. 3 Probability density function (*left*) and cumulative distribution function (*right*) of random orientation of 12-base pair ssDNA oligomers in an aqueous solution with different ionic concentrations and surface charges. The proteins rotate between 0 (*horizontal*) and $\pi/2$ (*vertical*) degrees at the surface

face are stronger. The orientations also depend on the ionic concentration of the liquid, as the effect of Debye screening is significant. Figure 3 shows the probability density function (PDF) and cumulative distribution function (CDF) of random orientation of various DNA oligomers bound to the nanowire surface. The figure indicates the Gaussian distribution of random variables. In summary, the coefficients $A(x, y, \cdot)$, $\rho(x, y, \cdot)$ and $\varphi(x, y, \cdot)$ in (1) are random variables, i.e., $A(x, y, \omega)$, $\rho(x, y, \omega)$, and $\varphi(x, y, \omega)$ depend on an element $\omega = (\omega_1, \omega_2, \dots, \omega_n)$ of the underlying probability space (Ω, Σ, P) . The sample space Ω describes the locations of the probe molecules, the state of the probe molecules (bound to a target molecules or not), and the orientations of the probe molecules and probe–target complexes. The modeling and simulation results in [17,38] yield the probability measure P .

We assume that the number of probe molecules per unit area follows a Poisson distribution. Once the number N of probe molecules or binding sites and their positions are fixed, the sample space is

$$\Omega = (\{0, 1\} \times [0, \pi/2])^N,$$

where 0 denotes the absence of any target molecule, 1 the presence of a target molecule, and $\eta \in [0, \pi/2]$ is the angle of molecule.

3 Basis adaptation

It is clear from Fig. 1 and Sect. 2 that the quantity of interest I in (3) is a nonlinear functional of the potential u , the

solution of the stochastic semilinear elliptic equation (1). Furthermore, in order to obtain a reasonable estimation of the (expected value of) current, several evaluations are necessary, which are computationally speaking expensive. These facts motivate the use of basis adaptation [11] to solve (1).

3.1 Polynomial chaos expansion (PCE)

Generalized polynomial chaos (GPC) seeks to represent an approximation of a random function by a set of random variables and orthogonal polynomials. It estimates coefficients for known orthogonal polynomial basis functions based on a set of response-function evaluations using sampling, tensor-product quadrature, or Smolyak sparse-grid approaches [13]. The general idea of the expansion is to transfer randomness to the basis functions and to use Hermite polynomials as basis functions. A stochastic function like $u \in L^2(D, \Omega)$ can be explained as its Wiener–Hermite polynomial chaos expansion [41]:

$$u(x, \omega) := \sum_{\beta} u_{\beta}(x) \Phi_{\beta}(\omega). \tag{5}$$

Here, Φ_{β} is an orthonormal Hermit polynomial, $\beta = (\beta_1, \beta_2, \dots, \beta_n)$ is a vector of n nonnegative integers which describes the order of polynomials, $x \in D$, and ω is a vector of uncorrelated Gaussian random variables. In order to approximate the series (5), we truncate it to a finite number of terms for the sake of computation

$$u(x, \omega) := \sum_{\beta \in M_k} u_{\beta}(x) \Phi_{\beta}(\omega), \tag{6}$$

where the truncated index set

$$M_k = \{\boldsymbol{\beta} = (\beta_i, i \geq 1 \mid \beta_i \in \{0, 1, \dots, k\})\}$$

is used for the series. The function can be characterized by its expected value with respect to the probability space as

$$\mathbb{E}(u(\mathbf{x}, \boldsymbol{\omega})) = \int_{\Omega} u(\mathbf{x}, \boldsymbol{\omega})\mu(\boldsymbol{\omega})d\boldsymbol{\omega}, \tag{7}$$

where $\mu(\boldsymbol{\omega})$ is the probability density function (PDF) corresponding to random variable $\boldsymbol{\omega}$. By the Cameron–Martin theorem, GPC approximation of (6) is fully converged in L^2 norm if

$$\lim_{k \rightarrow \infty} \int_{\Omega} \left(\sum_{\boldsymbol{\beta} \in M_k} u_{\boldsymbol{\beta}}(\mathbf{x})\Phi_{\boldsymbol{\beta}}(\boldsymbol{\omega}) - u(\mathbf{x}, \boldsymbol{\omega}) \right) \mu(\boldsymbol{\omega})d\boldsymbol{\omega} = 0. \tag{8}$$

The general idea of our basis adaptation is rotating random variables and transferring them from uncorrelated to correlated random variables. To this end, we define an isometry $\mathcal{L} : \mathbb{R}^n \rightarrow \mathbb{R}^n$ to define new basis. Therefore, the rotated random variables are defined as

$$\boldsymbol{\gamma} := \mathcal{L}\boldsymbol{\omega}. \tag{9}$$

The solution of (1) under this isometry can be obtained by

$$u(\mathbf{x}, \boldsymbol{\gamma}) = \sum_{\boldsymbol{\beta} \in M_k} u_{\boldsymbol{\beta}}^{\mathcal{L}}(\mathbf{x})\Phi_{\boldsymbol{\beta}}(\mathcal{L}\boldsymbol{\omega}). \tag{10}$$

The calculation of the coefficients of the series is the main point which can be defined as

$$\begin{aligned} u_{\boldsymbol{\beta}}^{\mathcal{L}}(\mathbf{x}) &= \sum_{\boldsymbol{\delta} \in M_k} u_{\boldsymbol{\delta}}(\mathbf{x}) \langle \Phi_{\boldsymbol{\beta}}(\boldsymbol{\omega}), \Phi_{\boldsymbol{\delta}}^{\mathcal{L}}(\boldsymbol{\omega}) \rangle \\ &= \sum_{\boldsymbol{\delta} \in M_k} u_{\boldsymbol{\delta}}(\mathbf{x}) \langle \Phi_{\boldsymbol{\beta}}(\boldsymbol{\omega}), \Phi_{\boldsymbol{\delta}}(\boldsymbol{\gamma}) \rangle. \end{aligned} \tag{11}$$

The inner product in the Hilbert space is characterized by weight function as the probability density function relative to the Gaussian measure [41]. An important property of the polynomials which will be used in the following estimations is their orthogonality with respect to the Gaussian probability measure. Therefore, the orthogonality of polynomial basis can be used to simplify (11) as follows:

$$u_{\boldsymbol{\beta}}^{\mathcal{L}}(\mathbf{x}) = \sum_{\boldsymbol{\beta} \in M_k} u_{\boldsymbol{\beta}}(\mathbf{x}) \langle \Phi_{\boldsymbol{\beta}}(\boldsymbol{\omega}), \Phi_{\boldsymbol{\beta}}(\boldsymbol{\gamma}) \rangle. \tag{12}$$

The isometry \mathcal{L} still needs to be constructed in a suitable manner to transfer one basis ($\boldsymbol{\omega}$) to other basis ($\boldsymbol{\gamma}$). To construct the isometry \mathcal{L} , we use quadratic adaptation [36]. As the first step, we define a multi-index $\mathbf{q}_i = (0, \dots, 1, \dots, 0)$ where only the i th point is 1 and other elements are zero. The matrix \mathcal{L} is given by

$$\mathcal{L}^T \mathbf{D} \mathcal{L} = \mathbf{B}, \tag{13}$$

where the diagonal elements of \mathbf{B} are $b_{ii} = \frac{u_{2q_i}}{\sqrt{2}}$ and the rest of entries are $b_{ij} = \frac{u_{q_{ij}}}{\sqrt{2}}$. After this calculation, \mathcal{L} and \mathbf{D} , which are, respectively, eigenvectors and eigenvalues of matrix \mathbf{B} , can be calculated.

3.2 Application to the stochastic nonlinear Poisson–Boltzmann equation

In the application considered here, the random process is localized near the manifold that describes the surface of the sensor. Physically speaking, the free ions in the aqueous solution screen the effect of the charges of the biomolecules, whose movement is random. The distance where the field effect is still significant is given by (a multiple of) the Debye length. Mathematically speaking, the semilinear term in (1) results in an exponential decay of the solution away from a point charge. Therefore, the important uncertainty area of biomolecules is at the surface.

In Monte-Carlo sampling, the coefficients of (6) are estimated as follows:

$$u_{\boldsymbol{\beta}}(\mathbf{x}) = \frac{1}{M} \sum_{j=1}^M u(\mathbf{x}, \boldsymbol{\omega}^{(j)})\Phi_{\boldsymbol{\beta}}(\boldsymbol{\omega}^{(j)}), \tag{14}$$

where M is the number of evaluations and $\boldsymbol{\beta} \in M_k$. For the fluctuation of n target molecules at the surface, we calculate (10) as an approximation of (1) using the following formula:

$$\begin{aligned} u^{\mathcal{L}}(\mathbf{x}, \boldsymbol{\gamma}) &= u_0^{\mathcal{L}}(\mathbf{x}) + \sum_{i=1}^n u_i^{\mathcal{L}}(\mathbf{x})\gamma_i + \sum_{i=1}^n u_{ii}^{\mathcal{L}}(\mathbf{x}) \frac{\gamma_i^2 - 1}{\sqrt{2}} \\ &+ \sum_{\substack{\boldsymbol{\beta} \in M_k \\ k \geq 3}} \sum_{i=1}^n u_{\boldsymbol{\beta}_i}^{\mathcal{L}} \Phi_{\boldsymbol{\beta}}(\gamma_i), \end{aligned} \tag{15}$$

where the rotated random variables are as (9) and the coefficients are calculated by (12) and (14). The main advantage of the basis adaptation compared to full-dimensional variables ($\boldsymbol{\omega}$) is that with transformation of the chaos to Gaussian process, the cost of calculation decreases dramatically. In fact, in spite of truncation of (15), e.g., second-order adapted series, very good estimation of (1) can be achieved. In this work, the main goal is the calculation of electrical current

(quantity of interest). Hence, with respect to the transformation, it can finally be obtained by the following equation:

$$I(\boldsymbol{\gamma}) = f(u_{\beta}^{\mathcal{L}}(\mathbf{x}, \boldsymbol{\gamma})). \tag{16}$$

4 Multi-level Monte-Carlo method

We have also devised a multi-level Monte-Carlo (MLMC) method for this problem. Since numerical results comparing MLMC and basis adaptation will be shown in Sect. 5, a summary of our MLMC approach is given here. The multi-level approach to the Monte-Carlo method was introduced for stochastic ordinary differential equations first [14] and has been applied to stochastic partial differential equations since then [2,9].

The basic idea of MLMC is to use levels $\ell \in \{0, \dots, L\}$ with grids of different fineness h_ℓ in order to approximate the expectation $\mathbb{E}[u]$ of the solution u and to reduce the variance by combining the solutions at various levels. It is straightforward to see that

$$E[u_{h_L}] = \sum_{\ell=1}^L E[u_{h_\ell} - u_{h_{\ell-1}}]$$

holds after defining $E[u_{h_0}] := 0$. In multi-level Monte Carlo, the expectation $E[u_{h_\ell} - u_{h_{\ell-1}}]$ is approximated by a level-dependent number M_ℓ of samples, i.e., the estimator

$$E_{\text{MLMC}}[u] := \sum_{\ell=1}^L E_{\text{MC}}[u_{h_\ell} - u_{h_{\ell-1}}]$$

is used, where E_{MC} is the usual Monte-Carlo estimator. For the mesh refinement, we define the mesh size in level ℓ as

$$h_\ell = \frac{h_0}{2^\ell},$$

where h_0 denotes the mesh size of the coarsest triangulation. If an inequality of the form

$$\|\nabla[u_{h_\ell} - u_{h_{\ell-1}}]\|_{L^2(D)} \leq C_0^2 h_{\ell-1}^\alpha \quad \exists C_0 \in \mathbb{R}^+ \tag{17}$$

holds for the variance and an inequality of the form

$$\|E[u_{h_L} - u]\|_{L^2(D)} \leq C_1^2 h_L^\beta \quad \exists C_1 \in \mathbb{R}^+ \tag{18}$$

holds for the spatial discretization, then it can be shown that the estimate

$$\text{MSE}(u) \leq C_0^2 \sum_{\ell=0}^L M_\ell^{-1} h_\ell^\alpha + C_1^2 h_L^\beta \tag{19}$$

holds for the mean square error.

It is additionally possible to optimize the fineness of the grids, the number of samples at each level, and the number of levels. More precisely, one considers the minimization problem

$$\begin{aligned} & \underset{L \in \mathbb{N}, M_\ell, h_\ell \in \mathbb{R}^+}{\text{minimize}} && \sum_{\ell=0}^L M_\ell h_\ell^{-\gamma} \\ & \text{subject to} && C_0^2 \sum_{\ell=0}^L M_\ell^{-1} h_\ell^\alpha + C_1^2 h_L^\beta \leq \epsilon. \end{aligned} \tag{20}$$

Here, $L \in \mathbb{N}$, the terms $h_\ell^{-\gamma}$ denote the average cost at level ℓ , and ϵ is the given total error to be achieved. Then this minimization problem can be solved by numerical optimization methods, e.g., interior point. This yields the optimal MLMC method for a given spatial discretization method such as FEM of a given order, a given implementation, and a given error. Here, first of all we take advantage of multi-level Monte Carlo, i.e., variance reduction of random variables. Secondly, with optimized hierarchies of mesh size and number of samples, the lowest computational complexity (work) is achieved for a given ϵ . It provides an efficient alternative of Monte Carlo.

5 Numerical results

In order to assess the efficiency of the basis-adaptation method devised and also to compare it to the MLMC approach, the structure in Fig. 1 was considered with realistic parameter values. It corresponds to a cross section of a nanowire field-effect biosensor. To verify our stochastic methods, the statistical parameters of quantity of interests (current) are compared. To this end, we compare the expected value of current ($\mathbb{E}(I)$) with respect to different physical parameters, e.g., ionic concentration, doping concentration. Moreover, we define signal-to-noise ratio (SNR) of current as

$$\text{SNR}(I) := \frac{\mathbb{E}(I)}{\sqrt{\text{Var}(I)}},$$

where $\text{Var}(I)$ indicates the variance of quantity of interest. The ratio enables us to study the effect of the parameters on the biological noise, i.e., random movement of biomolecules at the surface.

When quantifying noise and fluctuations in sensors, various situations where different types of molecules are present should be considered. Probe molecules are functionalized at the sensor surface [32] when the sensor is manufactured and thus they are responsible for selectivity. In the case of DNA sensors, the probe molecules may be single-stranded peptide-nucleic-acid (PNA) oligomers, which are uncharged, or ssDNA oligomers, which are highly charged. The probe

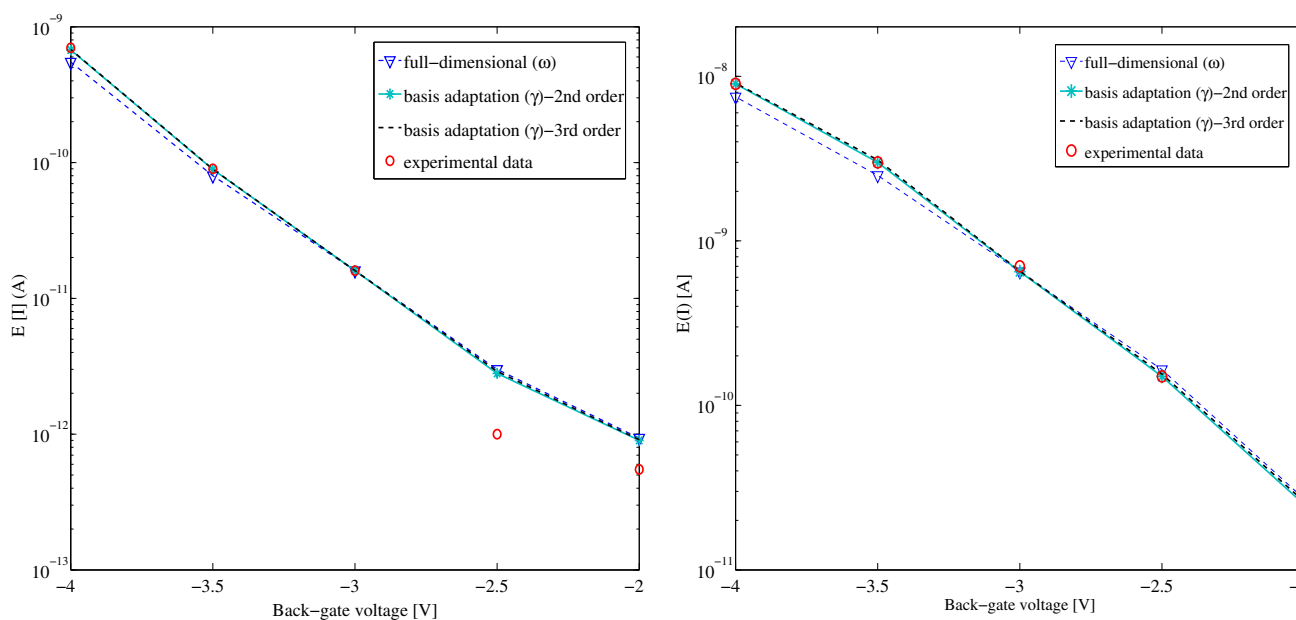


Fig. 4 Comparison of measured and simulated current (expected value) in respect of different back-gate voltages for 60-nm (*left*) and 100-nm (*right*) widths of transducer. The simulations are performed for the reference structure, where the back-gate voltage was varied

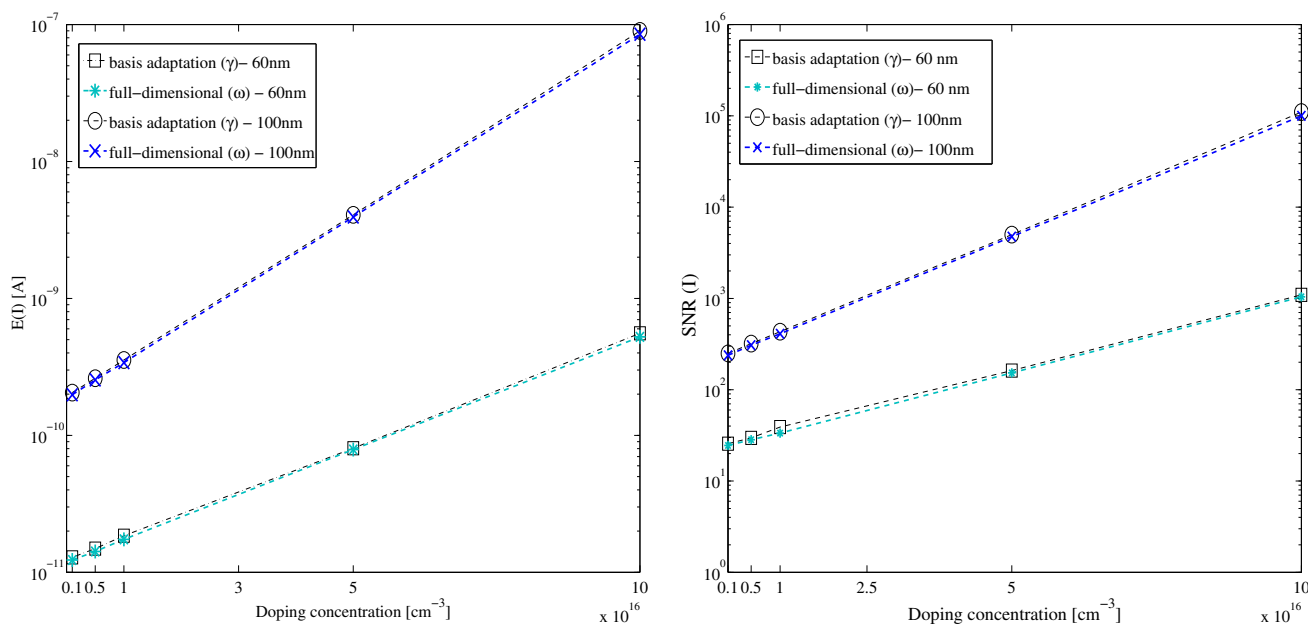


Fig. 5 Expected value of current and its signal-to-noise ratio as functions of doping concentration for 60-nm and 100-nm-wide devices. Here, the ionic concentration is 30 mM; the surface charge is -0.5 q nm^{-2} ; the oligomer length is 12 base pairs; $V_{BG} = -3 \text{ V}$; and the thermal voltage is 0.021 V

molecules move randomly, although there are preferred orientations, which have been calculated [17]. Target molecules bind to the probe molecules and are detected by the field effect modeled here. In the case of a DNA sensor, ssDNA oligomers bind to ssDNA or PNA oligomers. Binding and unbinding are stochastic processes [38]. Here we consider the leading example of a DNA sensor with ssDNA oligomers as

probe molecules and ssDNA oligomers as target molecules. The double-stranded probe-target complex carries twice the charge of a single strand. These considerations give the stochastic coefficients in (1).

The sizes in the various subdomains in Fig. 1 were determined by the following considerations. As found in [5], the optimal width of the silicon transducer is certainly smaller

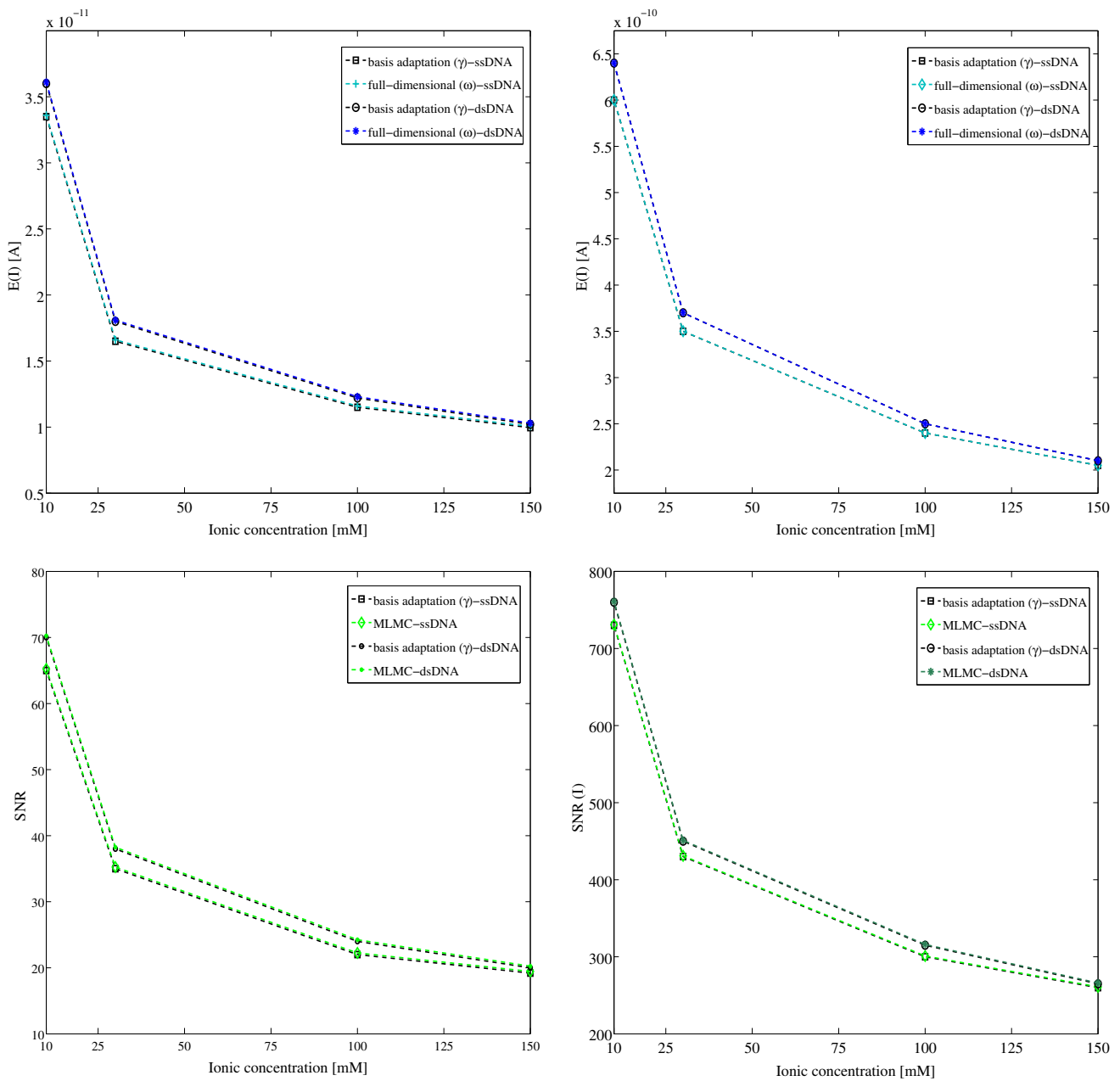


Fig. 6 Comparison of expected value (*top*) and signal-to-noise ratio of current (*bottom*) for 60-nm (*left*) and 100-nm (*right*) widths as functions of ionic concentration. Here, the doping concentration is 10^{16} cm^{-3} ;

the surface charge is -0.5 q nm^{-2} ; the oligomer length is 12 base pairs; $V_{BG} = -3 \text{ V}$; and the thermal voltage is 0.021 V

than 100 nm, while its precise value depends on other parameters such as the applied back-gate voltage. Smaller geometries were found to have higher sensitivity.

In order to validate the basis-adaptation approach, two nanowires with different widths are compared and shown in Fig. 4. The geometry of the sensor is shown in Fig. 1, where the thickness of the oxide layer is 8 nm and the thickness of the nanowire is 50 nm. For the simulations, we define a reference structure, where the back-gate voltage (V_{BG})

is -3 V ; the solution voltage is 0 V ; $u_S - u_D$ is 0.2 V ; the length of the nanowire is 1000 nm; the ionic concentration is 30 mM; the surface charge is -0.5 q nm^{-2} ; the doping concentration is 10^{16} cm^{-3} ; the oligomers consist of 12 base pairs; and the thermal voltage is 0.021 V . The length of each base pair is 0.34 nm. Furthermore, the electron mobility is $1000 \text{ cm}^2 \text{ V}^{-1} \text{ s}^{-1}$, and the hole mobility is $100 \text{ cm}^2 \text{ V}^{-1} \text{ s}^{-1}$. The model is validated by comparison with experimental data (using the same data as in [5]).

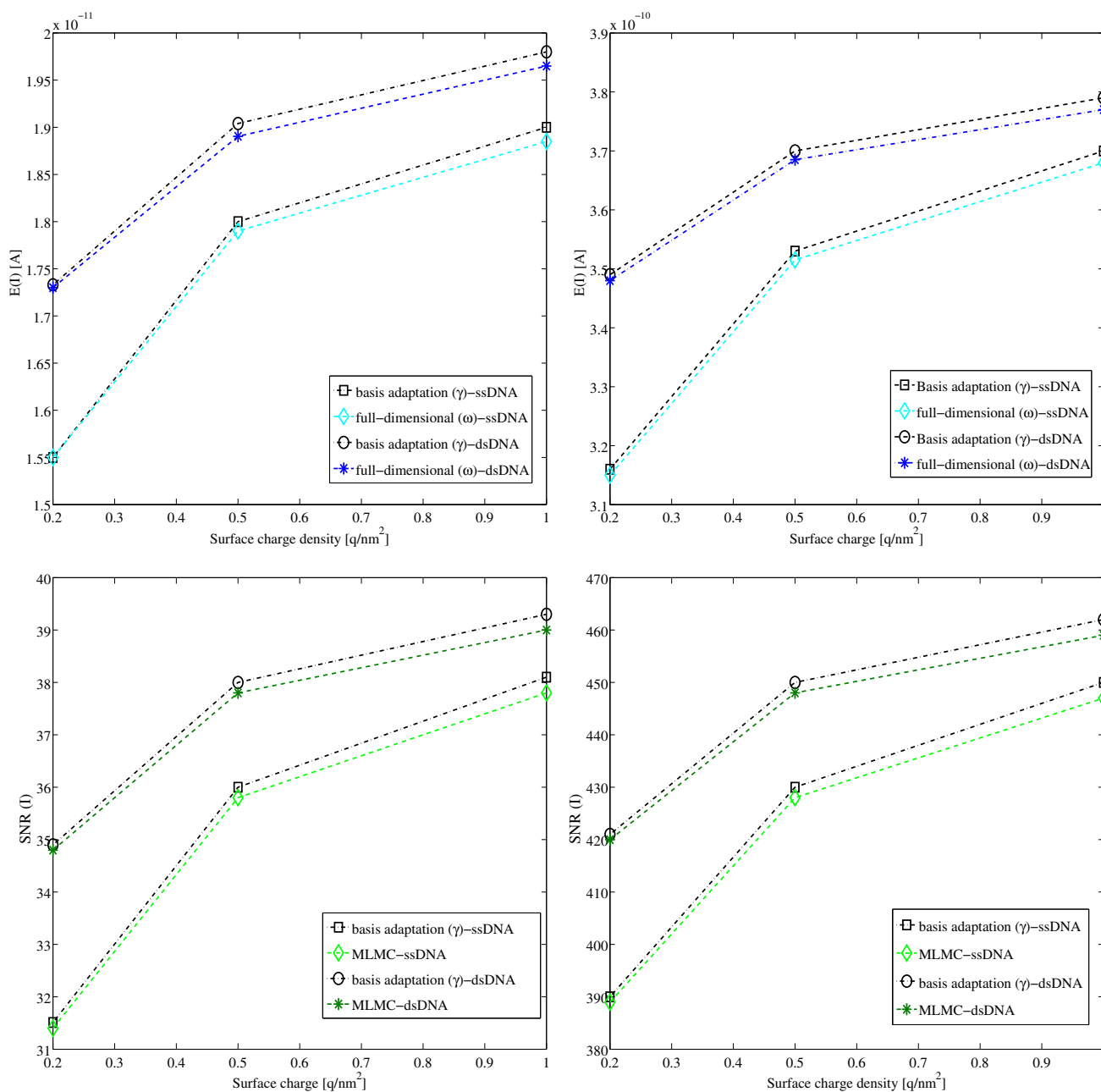


Fig. 7 Comparison of expected value (*top*) and the signal-to-noise ratio of the current (*bottom*) for 60-nm (*left*) and 100-nm (*right*)-wide sensors as functions of surface charge density. Here, the doping concentration

is 10^{16} cm⁻³; the ionic concentration is 30 nm; the oligomer length is 12 base pairs; $V_{BG} = -3$ V; and the thermal voltage is 0.021 V

The good agreement shows that the current calculated by the graded-channel approximation in Sect. 2.2 works very well for this kind of device due to its long length. Secondly, the solutions obtained by basis adaptation are compared with full-dimensional solutions.

The basis-adaptation approximation is obtained using a second-order polynomial chaos expansion of (15). The full-dimensional solution is the benchmark and actually

results from Hermite polynomial chaos expansion up to order 2. Here, the simulations are for fluctuations of 10 target molecules ($n = 10$) and 1000 Monte-Carlo replications ($M = 1000$). The agreement suggests that the implementation is correct. The differences between the full-dimensional solutions and the solutions obtained by basis adaptation become larger as the absolute value of the back-gate voltage increases; this is due to the fact that small differences

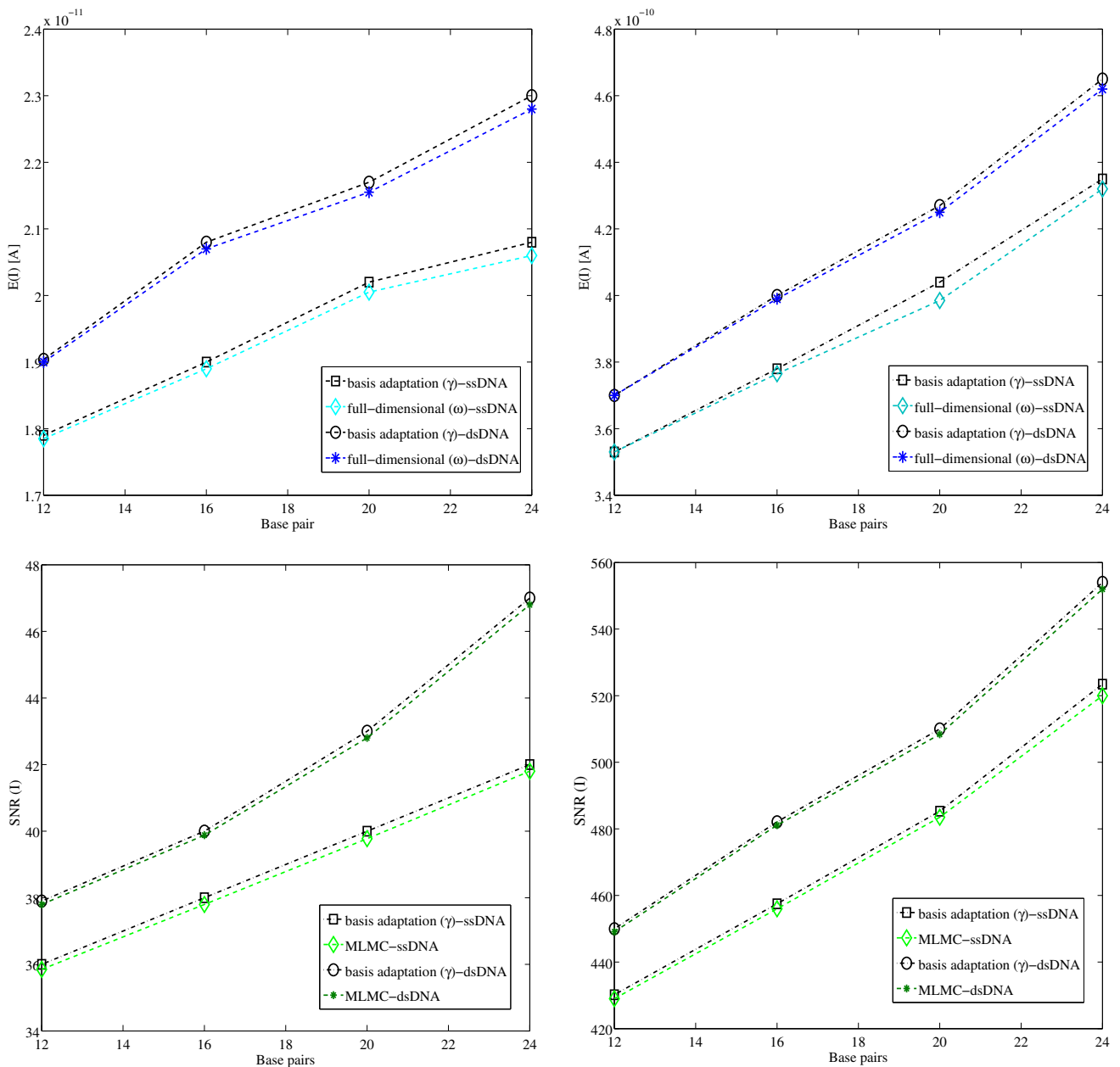


Fig. 8 Comparison of mean value (*top*) through the transducer and the signal-to-noise ratio of the current (*bottom*) for 60-nm (*left*) and 100-nm (*right*) widths as functions of oligomer length. Here, the doping

concentration is 10^{16} cm^{-3} ; the ionic concentration is 30 nm; the surface charge is -0.5 q nm^{-2} ; $V_{BG} = -3 \text{ V}$; and the thermal voltage is 0.021 V

are amplified by the large applied potential. The results are shown in Fig. 4. In the basis adaptation, the difference between second-order and third-order of PCE for both 60- and 100-nm-wide nanowires was negligible; therefore, second-order is used for all expected value and noise calculation in subsequent simulations. The results indicate the efficiency and the exactness of the basis adaptation against the full solution. The agreement with experimental data is very good and again justifies the model equations.

In this work, we also apply MLMC as another effective numerical technique. In different levels, optimized mesh sizes and number of realizations are obtained by solving the optimization problem (20). The coefficients of (17) and (18) are regarding the convergence of expected value and variance. The total error consists of discretization (spatial) error and statistical errors where the corresponding exponents are $\alpha \approx 3.2$ and $\beta \approx 1.7$. The coefficient γ is related to the dimension of the computational domain

($D \subset \mathbb{R}^2$). The hierarchies are obtained for the lowest cost of calculation such that the constraint (MSE) is satisfied for $\epsilon = 0.001$.

The stochastic equation (1) makes it possible to calculate higher-order moments and in particular the signal-to-noise ratio, an important characteristic value. In the following, we discuss how various important device parameters influence the quantity of interest, i.e., the current, and the signal-to-noise ratio. These simulations cover a large part of the parameter space and hence answer the question whether basis adaptation is generally useful or only for the choice of parameters in the previous figures.

The first parameter investigated here is the doping concentration. Currents were calculated for doping concentrations between 10^{15} and 10^{17} cm^{-3} and are shown in Fig. 5. The results show that both the current and the signal-to-noise ratio increase for 60- and 100-nm-wide transducers as the doping concentration increases. This means that higher doping concentrations not only increase the total current, but they also improve the signal compared to the noise, yielding a better sensor.

The second parameter considered here is the ionic concentration. It plays a crucial role, since a higher ionic concentration leads to higher screening and thus reduces the effectiveness of field-effect sensing. On the other hand, a certain ionic concentration (at least about 10 mM) is usually necessary—especially in the case of DNA—to enable probe–target binding. A Monte-Carlo algorithm to find the concentration of (counter) ions around biomolecules was developed in [7], and the ramifications of screening and how to overcome them were discussed in [21, 24]. For a typical salt concentration of 100 mM, the Debye length is approximately 1 nm and any charge is completely screened at a distance of only a few nanometers.

The numerical results in Fig. 6 show that the effect of the intrinsic charges of the target molecules on charge transport in the transducer is still measurable. Furthermore, the wider nanowire is more affected by screening within the semiconductor. Additionally, the signal-to-noise ratio in the 100-nm-wide transducer is increased by a factor of 10 compared to the 60-nm-wide device. Here, the ionic concentration varies between 10 and 150 mM.

The third parameter investigated here is the surface (fixed) charge of molecules. The surface charge is important since it determines the operating point of the sensor, which has a crucial influence on the sensitivity of the sensor [5]. Furthermore, a more negative surface charge repels target DNA oligomers, again emphasizing the necessity of considering the system in a self-consistent manner. In Fig. 7, the difference between ssDNA and dsDNA oligomers is clearly seen in both 60- and 100-nm-wide devices, as expected. The width of the device has a strong influence on current and signal-to-noise ratio. The current is about twenty times larger in the

wider device, while the signal-to-noise ratio is approximately twelve times larger.

The fourth and final parameter varied here is the length (and hence charge) of the DNA oligomers. The oligomers in the reference structure considered here are 12-base pairs long. However, depending on the application, the length of the probe and target oligomers may be varied. Figure 8 illustrates that increasing the oligomer length increases the current as well as the signal-to-noise ratio.

6 Conclusions

In all the numerical results, a very good agreement between basis adaptation and the full solution was found. This is true for a wide range of parameter values: doping concentration, ionic concentration, surface charge, and size and charge of molecules which were varied over large intervals. These numerical results show the effectiveness of basis adaptation for the stochastic nonlinear Poisson–Boltzmann equation.

The effectiveness of basis adaptation is due to the transformation of random variables and the properties of solutions of the (stochastic) nonlinear Poisson–Boltzmann equation. In particular, it is known that pointwise estimates hold for this type of semilinear problem [3, Lemma 3.2], [25], justifying the transformation of the basis of stochastic process.

Basis adaptation was also compared to a multi-level Monte-Carlo method as an example of another modern numerical approach for computing expected values of solutions of stochastic partial differential equations. In this problem, multi-level Monte Carlo performs well, but not as good as the basis adaptation. This is mainly due to the fact that the particular multi-level Monte-Carlo method used here does not take into account the special structure of the model equation, whereas the basis adaptation by the rotated random variables does. Ideas from the multi-level Monte-Carlo approach adapted to the problem at hand may increase the performance considerably specifically when the mesh sizes and number of evaluations are optimized.

Finally, an efficient numerical method for this equation makes it possible to perform simulations of realistic structures. Regarding the application of nanowire field-effect sensors, where the nonlinear Poisson–Boltzmann equation plays an important role as a fundamental model equation, a very good agreement of the basis-adaptation method with measurements was found. The stochastic nonlinear Poisson–Boltzmann equation makes it possible to include noise and fluctuations in the modeling, and the numerical results show how the various parameters affect the size of the signal and the signal-to-noise ratio, an important characteristic value of sensors. Also, we compared the influence of the width of two devices, where it was found that the 100-nm-wide sensor has a larger SNR than the 60-nm-wide one.

Acknowledgments The authors acknowledge the support by FWF (Austrian Science Fund) START Project No. Y660 *PDE Models for Nanotechnology*. The authors also would like to appreciate Prof. Roger Ghanem (University of Southern California) for useful discussions about polynomial chaos expansion.

References

- Alexander, C., Roy, G., Asenov, A.: Random-dopant-induced drain current variation in nano-MOSFETs: a three-dimensional self-consistent Monte Carlo simulation study using “ab initio” ionized impurity scattering. *IEEE Trans. Electron Devices* **55**(11), 3251–3258 (2008)
- Barth, A., Schwab, C., Zollinger, N.: Multi-level Monte Carlo finite element method for elliptic PDEs with stochastic coefficients. *Numer. Math.* **119**(1), 123–161 (2011)
- Baumgartner, S., Heitzinger, C.: Existence and local uniqueness for 3D self-consistent multiscale models for field-effect sensors. *Commun. Math. Sci.* **10**(2), 693–716 (2012)
- Baumgartner, S., Heitzinger, C.: A one-level FETI method for the drift-diffusion-Poisson system with discontinuities at an interface. *J. Comput. Phys.* **243**, 74–86 (2013). doi:10.1016/j.jcp.2013.02.043
- Baumgartner, S., Heitzinger, C., Vacic, A., Reed, M.A.: Predictive simulations and optimization of nanowire field-effect PSA sensors including screening. *Nanotechnology* **24**(22), 225503 (2013)
- Brunet, E., Maier, T., Mutinati, G., Steinhauer, S., Köck, A., Gspan, C., Grogger, W.: Comparison of the gas sensing performance of SnO₂ thin film and SnO₂ nanowire sensors. *Sens. Actuators B* **165**(1), 110–118 (2012)
- Bulyha, A., Heitzinger, C.: An algorithm for three-dimensional Monte-Carlo simulation of charge distribution at biofunctionalized surfaces. *Nanoscale* **3**(4), 1608–1617 (2011)
- Chen, D., Wei, G.W.: Modeling and simulation of electronic structure, material interface and random doping in nano-electronic devices. *J. Comput. Phys.* **229**(12), 4431–4460 (2010)
- Cliffe, K., Giles, M., Scheichl, R., Teckentrup, A.L.: Multilevel Monte Carlo methods and applications to elliptic PDEs with random coefficients. *Comput. Vis. Sci.* **14**(1), 3–15 (2011)
- Cui, Y., Wei, Q., Park, H., Lieber, C.M.: Nanowire nanosensors for highly sensitive and selective detection of biological and chemical species. *Science* **293**(5533), 1289–1292 (2001)
- Doostan, A., Ghanem, R.G., Red-Horse, J.: Stochastic model reduction for chaos representations. *Comput. Methods Appl. Mech. Eng.* **196**(37), 3951–3966 (2007)
- Duan, X., Li, Y., Rajan, N.K., Routenberg, D.A., Modis, Y., Reed, M.A.: Quantification of the affinities and kinetics of protein interactions using silicon nanowire biosensors. *Nat. Nanotechnol.* **7**(6), 401–407 (2012)
- Eldred, M., Burkardt, J.: Comparison of non-intrusive polynomial chaos and stochastic collocation methods for uncertainty quantification. In: *Proc. 47th AIAA Aerospace Sciences Meeting*, vol. 976, pp. 1–20 (2009)
- Giles, M.: Improved multilevel Monte Carlo convergence using the Milstein scheme. *Monte Carlo and Quasi-Monte Carlo Methods 2006*, pp. 243–258. Springer, Berlin (2008)
- Hahn, J., Lieber, C.M.: Direct ultrasensitive electrical detection of DNA and DNA sequence variations using nanowire nanosensors. *Nano Lett.* **4**(1), 51–54 (2004)
- Hassibi, A., Navid, R., Dutton, R., Lee, T.: Comprehensive study of noise processes in electrode electrolyte interfaces. *J. Appl. Phys.* **96**(2), 1074–1082 (2004)
- Heitzinger, C., Liu, Y., Mauser, N.J., Ringhofer, C., Dutton, R.W.: Calculation of fluctuations in boundary layers of nanowire field-effect biosensors. *J. Comput. Theor. Nanosci.* **7**(12), 2574–2580 (2010)
- Heitzinger, C., Mauser, N.J., Ringhofer, C.: Multiscale modeling of planar and nanowire field-effect biosensors. *SIAM J. Appl. Math.* **70**(5), 1634–1654 (2010)
- Heitzinger, C., Ringhofer, C.: Multiscale modeling of fluctuations in stochastic elliptic PDE models of nanosensors. *Commun. Math. Sci.* **12**(3), 401–421 (2014). doi:10.4310/CMS.2014.v12.n3.a1
- Köck, A., Tischner, A., Maier, T., Kast, M., Edtmaier, C., Gspan, C., Kothleitner, G.: Atmospheric pressure fabrication of SnO₂-nanowires for highly sensitive CO and CH₄ detection. *Sens. Actuators B* **138**(1), 160–167 (2009)
- Kulkarni, G.S., Zhong, Z.: Detection beyond the Debye screening length in a high-frequency nanoelectronic biosensor. *Nano Lett.* **12**(2), 719–723 (2012)
- Laborde, C., Pittino, F., Verhoeven, H., Lemay, S., Selmi, L., Jongasma, M., Widdershoven, F.: Real-time imaging of microparticles and living cells with nanocapacitor arrays. *Nat. Nanotechnol.* **10**, 791–795 (2015)
- Lee, A., Brown, A.R., Asenov, A., Roy, S.: Random telegraph signal noise simulation of decanano MOSFETs subject to atomic scale structure variation. *Superlattices Microstruct.* **34**(3), 293–300 (2003)
- Liu, Y., Lilja, K., Heitzinger, C., Dutton, R.W.: Overcoming the screening-induced performance limits of nanowire biosensors: a simulation study on the effect of electro-diffusion flow. In: *IEDM 2008 Technical Digest*, pp. 491–494. San Francisco, CA (2008). doi:10.1109/IEDM.2008.4796733
- Markowich, P., Ringhofer, C., Schmeiser, C.: *Semiconductor*. Springer, Wien (1990)
- Patolsky, F., Timko, B.P., Yu, G., Fang, Y., Greytak, A.B., Zheng, G., Lieber, C.M.: Detection, stimulation, and inhibition of neuronal signals with high-density nanowire transistor arrays. *Science* **313**(5790), 1100–1104 (2006)
- Patolsky, F., Zheng, G., Lieber, C.M.: Fabrication of silicon nanowire devices for ultrasensitive, label-free, real-time detection of biological and chemical species. *Nat. Protoc.* **1**(4), 1711–1724 (2006)
- Pittino, F., Selmi, L.: Use and comparative assessment of the CVFEM method for Poisson–Boltzmann and Poisson–Nernst–Planck three dimensional simulations of impedimetric nanobiosensors operated in the DC and AC small signal regimes. *Comput. Methods Appl. Mech. Eng.* **278**, 902–923 (2014)
- Pittino, F., Palestri, P., Scarbolo, P., Esseni, D., Selmi, L.: Models for the use of commercial TCAD in the analysis of silicon-based integrated biosensors. *Solid-State Electron.* **98**, 63–69 (2014)
- Pittino, F., Passerini, F., Selmi, L., Widdershoven, F.: Numerical simulation of the position and orientation effects on the impedance response of nanoelectrode array biosensors to DNA and PNA strands. *Microelectron. J.* **45**(12), 1695–1700 (2014)
- Ponzoni, A., Comini, E., Sberveglieri, G., Zhou, J., Deng, S.Z., Xu, N.S., Ding, Y., Wang, Z.L.: Ultrasensitive and highly selective gas sensors using three-dimensional tungsten oxide nanowire networks. *Appl. Phys. Lett.* **88**(20), 203,101 (2006)
- Punzet, M., Baurecht, D., Varga, F., Karlic, H., Heitzinger, C.: Determination of surface concentrations of individual molecule-layers used in nanoscale biosensors by in situ ATR-FTIR spectroscopy. *Nanoscale* **4**(7), 2431–2438 (2012)
- Rajan, N.K., Routenberg, D.A., Reed, M.A.: Optimal signal-to-noise ratio for silicon nanowire biochemical sensors. *Appl. Phys. Lett.* **98**(26), 264,107 (2011)
- Stern, E., Klemic, J.F., Routenberg, D.A., Wyrembak, P.N., Turner-Evans, D.B., Hamilton, A.D., LaVan, D.A., Fahmy, T.M., Reed, M.A.: Label-free immunodetection with CMOS-compatible semiconducting nanowires. *Nature* **445**(7127), 519–522 (2007)

35. Stern, E., Vacic, A., Rajan, N.K., Criscione, J.M., Park, J., Ilic, B.R., Mooney, D.J., Reed, M.A., Fahmy, T.M.: Label-free biomarker detection from whole blood. *Nat. Nanotechnol.* **5**(2), 138–142 (2010)
36. Tipireddy, R., Ghanem, R.: Basis adaptation in homogeneous chaos spaces. *J. Comput. Phys.* **259**, 304–317 (2014)
37. Tulzer, G., Baumgartner, S., Brunet, E., Mutinati, G.C., Steinhauer, S., Köck, A., Barbano, P.E., Heitzinger, C.: Kinetic parameter estimation and fluctuation analysis of CO at SnO₂ single nanowires. *Nanotechnology* **24**(31), 315501 (2013)
38. Tulzer, G., Heitzinger, C.: Fluctuations due to association and dissociation processes at nanowire-biosensor surfaces and their optimal design. *Nanotechnology* **26**(2), 025502 (2015). doi:[10.1088/0957-4484/26/2/025502](https://doi.org/10.1088/0957-4484/26/2/025502)
39. Uren, M., Day, D., Kirton, M.: 1/f and random telegraph noise in silicon metal-oxide-semiconductor field-effect transistors. *Appl. Phys. Lett.* **47**(11), 1195–1197 (1985)
40. Wang, C., Yin, L., Zhang, L., Xiang, D., Gao, R.: Metal oxide gas sensors: sensitivity and influencing factors. *Sensors* **10**(3), 2088–2106 (2010)
41. Xiu, D., Karniadakis, G.E.: The Wiener–Askey polynomial chaos for stochastic differential equations. *SIAM J. Sci. Comput.* **24**(2), 619–644 (2002)
42. Zheng, G., Patolsky, F., Cui, Y., Wang, W.U., Lieber, C.M.: Multiplexed electrical detection of cancer markers with nanowire sensor arrays. *Nat. Biotechnol.* **23**(10), 1294–1301 (2005)